Journal of Scientific Computing, Vol. 19, Nos. 1–3, December 2003 (© 2003)

A Level Set Approach for the Numerical Simulation of Dendritic Growth

Frédéric Gibou,[1] Ronald Fedkiw,[2] Russel Caflisch,[3] and Stanley Osher[3]

Received April 24, 2002; accepted (in revised form) October 17, 2002

In this paper, we present a level set approach for the modeling of dendritic solidification. These simulations exploit a recently developed second order accurate symmetric discretization of the Poisson equation, see [12]. Numerical results indicate that this method can be used successfully on complex interfacial shapes and can simulate many of the physical features of dendritic solidification. We apply this algorithm to the simulation of the dendritic crystallization of a pure melt and find that the dendrite tip velocity and tip shapes are in excellent agreement with solvability theory. Numerical results are presented in both two and three spatial dimensions.

KEY WORDS: Interfaces; level set method; ghost fluid method; Poisson equation; dendritic growth.

1. INTRODUCTION

Various numerical methods have been developed to solve the difficult problems associated with dendritic crystallization. Broadly speaking, there are two issues that a successful numerical technique must address. First, it needs to track a topologically complex, moving solid-liquid interface in both two and three spatial dimensions. Second, it must be computationally efficient as these problems are usually parabolic in nature with stringent restrictions on the time step and small spatial scales that require sufficient grid resolution. Thus, a desirable scheme should use implicit time stepping with a symmetric inversion matrix as well as high order accurate spatial discretizations of both the parabolic partial differential equation and the interface itself.

The interface that separates the two phases can be tracked either explicitly or implicitly. The main disadvantage of an explicit approach, e.g., front tracking (see, e.g., [17]), is that special care is needed for topological changes such as merging or breaking. While this is easily overcome in two spatial dimensions, explicitly treating

[1] Mathematics Department & Computer Science Department, Stanford University, Stanford, California 94305. E-mail: fgibou@math.Stanford.edu
[2] Computer Science Department, Stanford University, Stanford, California 94305.
[3] Mathematics Department, University of California, Los Angeles, California 90095-1555.

0885-7474/03/1200-0183/0 © 2003 Plenum Publishing Corporation

connectivity in three spatial dimensions can be daunting. Implicit representations such as level set [26] or phase-field [18] methods represent the front as a level set of a continuous function. Topological changes are consequently handled in a straightforward fashion, and thus the methods are readily implemented in both two and three spatial dimensions. Moreover, one can easily model additional physics, e.g., material strain or flow past dendrites. Sometimes Eulerian methods, such as the level set method, are criticized for not accurately preserving the mass of a material. However, this artifact has recently been removed for level set methods with the aid of massless marker particles that obtain the accuracy benefits of a front tracking method without the added hindrance of addressing connectivity, see [8]. Moreover, in [9], the particle level set method developed in [8] was used to track topologically complex air/water interfaces subject to a variety of pinching and merging. These accuracy limitations have not yet been addressed for phase-field methods, but we are optimistic that the nonphysical mass loss present in phase-field methods can be alleviated to a large degree using a method similar to that proposed in [8].

A simple level set approach to solving the sharp interface problem described in Sec. 2.2 later was first proposed in [5]. They used the level set method to keep track of the front and solved for the diffusion field using an implicit time discretization method. In order to apply this implicit time discretization a constant coefficient matrix needs to be inverted at every time step. Their matrix was nonsymmetric and they used a rather slow Gauss–Seidel iterative scheme to invert limiting both the grid resolution and the number of spatial dimensions, i.e., they were not able to address Stefan problems in three spatial dimensions. In [21], the authors improved upon the algorithm presented in [5], for example computing the velocity in a more accurate manner. They numerically simulated the standard four-fold anisotropy test case, and obtained results in excellent agreement with the predictions of microscopic solvability theory.

In both [5] and [21] the discretization of the temperature near the interface produces a non-symmetric matrix that needs to be inverted for implicit time stepping. The lack of symmetry makes this approach computationally expensive, although methods like GMRES [29] and BICGSTAB [29] might help to alleviate the situation. In [10], a symmetric second order accurate discretization for the Poisson equation was originally developed and later presented and shown to be second order accurate in [12]. This algorithm was inspired by the ghost fluid method [11] and has been successfully used by a variety of authors (e.g., [6]). Applying this discretization technique to the temperature field near the interface allows one to use a robust and efficient Preconditioned Conjugate Gradient (PCG) [13] method to invert the constant coefficient matrix resulting from the implicit discretization in time (this algorithm is to be contrasted with [22] where the authors obtained only first order accuracy in the presence of a jump condition. Here second order accuracy is obtained for the Dirichlet boundary condition). In [12], numerical results showed that this scheme is second order accurate for the variable coefficient and constant coefficient Poisson equation and the heat equation. In particular, we showed that this new algorithm converges to some known exact solutions, e.g., the Frank-Sphere. In this paper, we apply this algorithm to the

modified Stefan problem taking into account crystalline anisotropy, surface tension and molecular kinetics.

The main difference between the phase-field and level set approach is that the level set method can be used to exactly locate the interface in order to apply discretizations that depend on the exact interface location. In contrast, the phase-field method only has an approximate representation of the front location and thus the discretization of the diffusion field is less accurate near the front resembling an enthalpy method [7]. Formulating a phase-field model requires an asymptotic expansion analysis be performed with a small parameter proportional to the interface width, W. It is important to note that the grid size is proportional to W and only in the limit as $W \to 0$ does the phase-field method converge to the sharp interface model. In that sense, the phase-field method is only a first order accurate approximation to the true macroscopic sharp interface model. That is, even if the numerics are second order accurate for a given value of W, the model is in error by $W \sim O(\triangle x)$ so that the method can be no better than first order accurate overall. In fact in [20] it was shown rigorously that if the grid size is not proportional to W, the numerical results are generally incorrect. The level set method does not need this extra level of adaptivity. The interested reader is referred to [18] and the references therein for more details on the phase-field method.

2. EQUATIONS AND NUMERICAL METHOD

2.1. Level Set Equation and Numerics

The level set equation

$$\phi_t + \vec{W} \cdot \nabla \phi = 0, \tag{1}$$

where ϕ is the level set function and $\vec{W}$ is the velocity field, is used to keep track of the interface location as the set of points where $\phi = 0$. The unreacted and reacted materials are then designated by the points where $\phi > 0$ and $\phi \leqslant 0$ respectively. To keep the values of ϕ close to those of a signed distance function, i.e., $|\nabla \phi| = 1$, the reinitialization equation introduced in [30]

$$\phi_\tau + S(\phi_o)(|\nabla \phi| - 1) = 0 \tag{2}$$

is iterated for a few steps in fictitious time, τ. Here $S(\phi_o)$ is a smoothed out sign function. The level set function is used to compute the normal $\vec{n} = \nabla \phi / |\nabla \phi|$ and the mean curvature $\kappa = \nabla \cdot \vec{n}$ in a standard fashion. The level set advection equation and the reinitialization equation are discretized by using the HJ-WENO type schemes [15], see also [23, 16]. For more details on the level set method see, e.g., [25, 24].

2.2. Sharp-Interface Model

Dendritic solidification that includes effects of undercooling, surface tension, crystalline anisotropy and molecular kinetics can be described by the sharp-interface model. Consider a Cartesian computational domain, Ω, with exterior boundary, $\partial\Omega$,

and a lower dimensional interface, Γ, that divides the computational domain into disjoint pieces, Ω^- and Ω^+. The sharp-interface model is given by

$$\frac{\partial T}{\partial t} = \nabla \cdot (v \nabla T) \qquad \vec{x} \in \Omega, \tag{3}$$

$$V_n = [v \nabla T \cdot \vec{n}] = (v \nabla T \cdot \vec{n})_r - (v \nabla T \cdot \vec{n})_u \qquad \vec{x} \in \Gamma, \tag{4}$$

where T denotes the temperature, $V_n = \vec{V} \cdot \vec{n}$ the normal velocity at the interface, and the subscripts u and r define the unreacted and reacted materials respectively (for example, in the case of a solidification process, the reacted material would be the solid and the unreacted one would be the melt bath). The thermal conductivity $v(\vec{x})$ is assumed continuous on each disjoint subdomain, Ω^- and Ω^+, but may be discontinuous across the interface Γ. Furthermore, $v(\vec{x})$ is assumed to be positive and bounded below by some $\epsilon > 0$. On the boundary of the computational domain, $\partial\Omega$, we consider either Dirichlet boundary conditions of $T(\vec{x}) = g(\vec{x})$ or Neumann boundary conditions of $\nabla T \cdot \vec{n}(\vec{x}) = h(\vec{x})$, although one could also consider periodic boundary conditions in a straight forward way. At the interface, we impose the Gibbs–Thomson relation

$$T_I = -\epsilon_c \kappa - \epsilon_v V_n, \tag{5}$$

where κ is the curvature of the front, ϵ_c the surface tension coefficient, ϵ_v the molecular kinetic coefficient and V_n the interface velocity. This interface condition accounts for the deviation of the interface temperature T_I from equilibrium. In the case where the surface tension at the interface is anisotropic, one can take for example in two spatial dimensions

$$\epsilon_c = d_0(1 - 15\epsilon \cos(4\alpha)), \tag{6}$$

where ϵ is the anisotropy strength, and α is the angle between the normal at the interface and the x-axis. This formula represents the standard four-fold anisotropy. The Gibbs–Thomson relation is computed at every grid point neighboring the interface and then linearly interpolated to the front using an easy to implement level set procedure, see [22]. When computing the Gibbs–Thomson relation, we use the value of the normal velocity V_n at time t^n.

In one spatial dimension, the discretization of the temperature is as follows. For grid points more than one grid cell away from the interface, we use a standard backward Euler implicit time discretization

$$\frac{T_i^{n+1} - T_i^n}{\triangle t} = \frac{v_{i+\frac{1}{2}} \left(\frac{T_{i+1}^{n+1} - T_i^{n+1}}{\triangle x} \right) - v_{i-\frac{1}{2}} \left(\frac{T_i^{n+1} - T_{i-1}^{n+1}}{\triangle x} \right)}{\triangle x} \tag{7}$$

which is second order accurate in space where the resolution of the interface is crucial, but only first order accurate in time. Moreover, second order accurate spatial resolution is desirable since Eq. (4) computes the interface velocity using the first derivatives of the temperature.

This discretization is not valid if the interface, Γ, cuts through the stencil of points: x_{i-1}, x_i and x_{i+1}. For example, suppose that the interface location, x_I, falls in between x_i and x_{i+1}. Then when discretizing at x_i, we do not have a valid value for T_{i+1} at x_{i+1} since T will generally have a kink across the interface (but may also be discontinuous in some models). We circumvent this difficulty by defining a ghost value of T^G_{i+1} at x_{i+1} rewriting Eq. (7) as

$$\frac{T_i^{n+1}-T_i^n}{\triangle t}=\frac{v_{i+\frac{1}{2}}\left(\frac{T^G_{i+1}-T_i^{n+1}}{\triangle x}\right)-v_{i-\frac{1}{2}}\left(\frac{T_i^{n+1}-T_{i-1}^{n+1}}{\triangle x}\right)}{\triangle x}. \tag{8}$$

With Dirichlet boundary conditions on the interface Γ, we can compute the interface temperature as T_I and use it to define the ghost value T^G_{i+1}. Then, possible candidates for T^G_{i+1} include

$$T^G_{i+1}=T_I, \tag{9}$$

$$T^G_{i+1}=\frac{T_I+(\theta-1)\,T_i}{\theta} \tag{10}$$

and

$$T^G_{i+1}=\frac{2T_I+(2\theta^2-2)\,T_i+(-\theta^2+1)\,T_{i-1}}{\theta^2+\theta} \tag{11}$$

corresponding to the use of constant, linear and quadratic extrapolation across the interface, respectively. Here $\theta=(x_I-x_i)/\triangle x$. Plugging Eq. (11) into Eq. (8) gives the standard second order accurate nonsymmetric discretization used by many authors, e.g., [5] and [21]. As pointed out in [12], this local quadratic extrapolation is unnecessary, however many authors still use it being misled by local Taylor expansion analysis. [12] showed that local linear extrapolation using Eq. (10) is enough to obtain second order spatial accuracy in the case where the exact interface location is known. Moreover, the resulting discretization is symmetric enabling the use of fast linear solvers such as PCG when employing implicit discretization in time. Plugging Eq. (10) into Eq. (8) gives a second order accurate symmetric discretization of

$$\frac{T_i^{n+1}-T_i^n}{\triangle t}=\frac{v_{i+\frac{1}{2}}\left(\frac{T_I-T_i}{\theta\,\triangle x}\right)-v_{i-\frac{1}{2}}\left(\frac{T_i-T_{i-1}}{\triangle x}\right)}{\triangle x}. \tag{12}$$

This is the scheme that we will use in the examples of Sec. 3. Note that since the temperature is computed to second order accuracy and $V_n=[\nabla T\cdot\vec{n}]$, the interface location is only first order accurate. Therefore in the case of a moving front the accuracy of the method first order. The Crank–Nicholson scheme would lower the truncation error but the scheme would still be first order accurate overall due to the calculation of the velocity field.

In certain situations, v may only be known at the grid nodes and the interface in which case $v_{i+\frac{1}{2}}$ in Eq. (8) is determined from a ghost value, v^G_{i+1}, and the usual averaging

$$v_{i+\frac{1}{2}} = \frac{v_i + v^G_{i+1}}{2} \tag{13}$$

noting that the ghost value is easily defined using linear extrapolation

$$v^G_{i+1} = \frac{v_I + (\theta - 1)\, v_i}{\theta} \tag{14}$$

according to Eq. (10).

In multiple spatial dimensions, the equations are discretized in a dimension by dimension manner using the one dimensional discretization outlined above. The interested reader is referred to [12] for the details of this method.

We find the interface normal velocity using the jump in the temperature gradient in the normal direction across the interface. Here again, we use the value of the temperature at the interface, T_I, and assume that the temperature profile is locally linear to compute the temperature gradient on each side of the interface. More precisely, we compute the derivatives T_x and T_y of the temperature in the x and y direction and then compute the temperature gradient in the normal direction $T_n = \nabla T \cdot \vec{n}$. Once T_n is defined at grid points adjacent to the interface, we extrapolate the values of $(T_n)_r$ from the reacted side of the interface to the unreacted side and extrapolate the values of $(T_n)_u$ from the unreacted side to the reacted side so that both $(T_n)_r$ and $(T_n)_u$ are defined at every grid point in a band about the interface. This is accomplished with constant extrapolation in the normal direction to the interface according to

$$I_\tau \pm n \cdot \nabla I = 0 \tag{15}$$

where I is the variable to be extrapolated and the equation is solved in fictitious time τ to steady state. This was first implemented in [5] using an equation that appears in [31]. This is done separately to advect $I = (T_n)_r$ in one direction and to advect $I = (T_n)_u$ in the other direction. Note that we do not solve Eq. (15) directly, but instead use an optimal spatial marching procedure [1] in order to obtain I local to the interface. See [12] for more details. Once both $(T_n)_r$ and $(T_n)_u$ are both defined at each grid node near the interface, we compute the jump in a node by node fashion using the nodal values of $(T_n)_r$ and $(T_n)_u$, i.e., $(V_n)_i = (vT_n)_{r,i} - (vT_n)_{u,i}$.

The time step restriction throughout this paper is given by

$$\triangle t = \min(\triangle t^H, \triangle t^L), \tag{16}$$

with

$$\triangle t^H = 0.5 \min(\triangle x, \triangle y, \triangle z) \tag{17}$$

chosen for accuracy considerations in the heat equation,

$$\Delta t^L \left(\frac{w_1}{\Delta x} + \frac{w_2}{\Delta y} + \frac{w_3}{\Delta z} \right) \leqslant 0.5, \tag{18}$$

with $\vec{W} = (w_1, w_2, w_3) = V_n \cdot \vec{n}$ chosen for stability of the level set equation.

3. NUMERICAL RESULTS

In [12] we addressed the simulations of a melt with constant temperature at the interface and compared our solutions to the Frank sphere exact solution. Here, we show that our method can take into account the different physical parameters needed to faithfully model crystal growth.

3.1. Topological Changes—Merging and Breaking

These two examples illustrate one of the main advantages of the level-set method, which is that it handles topological changes and complex interfacial shapes in a natural way. Figure 1 shows seven seeds growing under a constant normal

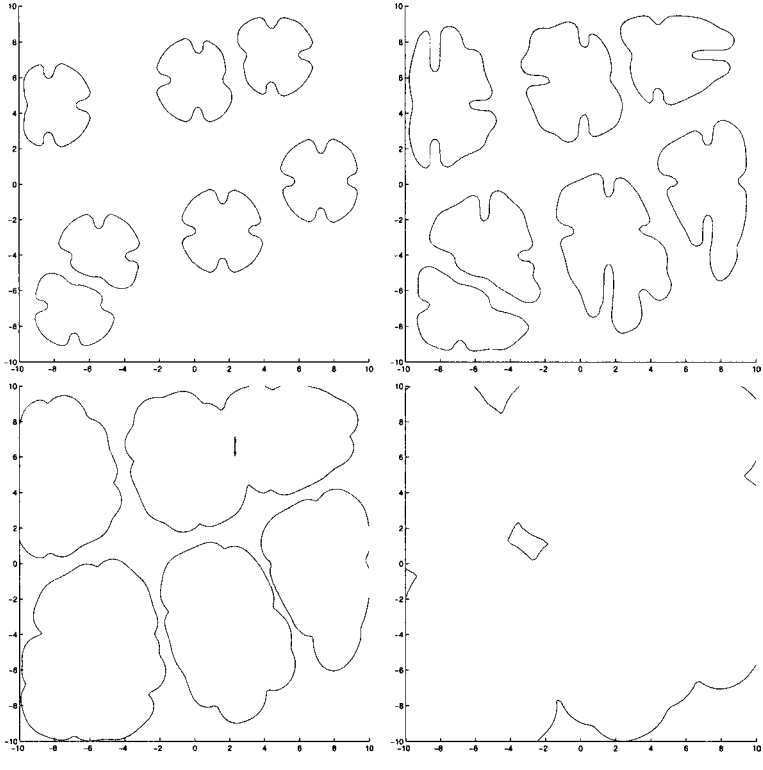

Fig. 1. Several seeds of arbitrary shapes grow under the normal velocity $v_n = 1$ and merge together. This example was ran with 100 grid points in each direction.

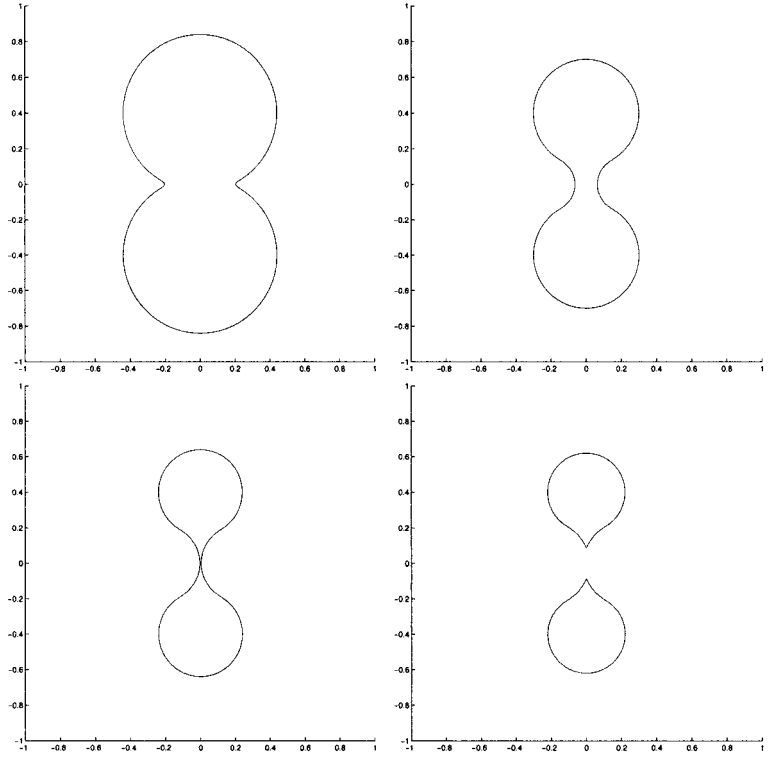

Fig. 2. A bulk of material is evolved with an interfacial normal velocity $v_n = -1$ and eventually breaks apart. This example was ran with 100 grid points in each direction.

velocity and merging. This characteristic has been exploited in the Islands-Dynamics model for epitaxial growth to model the merging of islands [4, 6, 28]. As a note, a constant velocity at the interface is physically relevant since, for example, it can model infinite edge diffusion at the interface of an island [4, 6, 28]. Figure 2 shows the breaking of crystals. In this example, a single crystal is shrunk with a negative constant normal velocity. This feature has been applied to the modeling of epitaxial growth to properly account for the thermal detachment of atoms from island edges, where island dissociation can occur [27]. The merging and the breaking of crystals are done automatically without any special treatments as opposed to what has to be done with explicit interface representations.

3.2. Effect of Varying Isotropic Surface Tension

Figure 3 demonstrates the effect of adding isotropic surface tension at the interface by imposing $T = -\epsilon_c \kappa$, and the corresponding smoothing effect on the crystal. Figure 3a depicts the evolution of a pure melt with $\epsilon_c = 0$. Since this case is

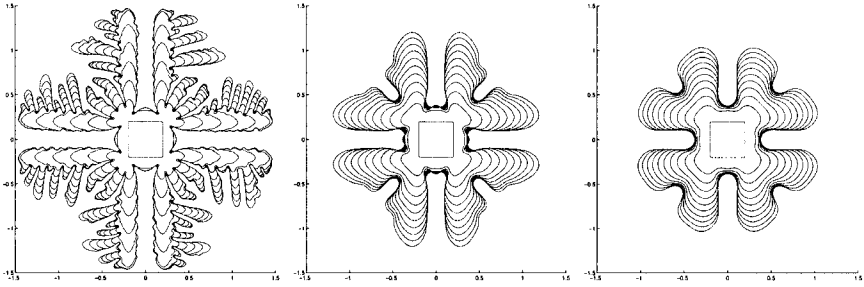

Fig. 3. Effect of varying isotropic surface tension. We impose the Gibbs–Thomson relation at the interface with $\epsilon_v = 0$ and (a) $\epsilon_c = 0$, (b) $\epsilon_c = 0.0005$, (c) $\epsilon_c = 0.001$. Grid sizes used are 300×300.

mathematically unstable, the regularization built-in to the level set method allows its calculation, see [14]. Our method seems to introduce less numerical diffusion than previous algorithms using the level set method, see [5] for a comparison. This comes in part from a higher order accuracy in the level set evolution. This translates into the more detailed dendrite structure obtained with our method. Figures 3b and c show the smoothing effect of increasing the surface tension at the interface.

3.3. Grid Refinement

This example, taken from [5], tests the convergence of our method under grid refinement. Consider a small frozen seed of material placed in a surrounding region of undercooled liquid with temperature $T_\infty = -0.5$. The computational domain is $[-2, 2] \times [-2, 2]$ and the initial shape is given in terms of the following parametric equations,

$$x(s) = (R + P\cos(8\pi s))\cos(2\pi s)$$
$$y(s) = (R + P\cos(8\pi s))\sin(2\pi s)$$

where $R = 0.1$, $P = 0.02$ and $s \in [0, 2\pi]$. We apply the Gibbs–Thomson relation, Eq. (5), at the interface with $\epsilon_c = 0.002$ and $\epsilon_v = 0.002$. For coarser grids, Fig. 4a, the numerical diffusion overcomes the physical regularization. However, as we refine the grid, the artificial numerical dissipation becomes negligible compared to the physical surface tension and the zero level set of ϕ converges to a similar shape. The convergence of these plots under grid refinement are comparable to those obtained by [5], but we achieve convergence with fewer grid points as our method has less artificial numerical dissipation, due to our use of more accurate numerical methods in a variety of places.

3.4. Effect of Anisotropic Surface Tension

Physical anisotropy forces a crystal to grow along preferred directions. In this example we impose the condition $T = -\epsilon_c \kappa$ at the interface with

$$\epsilon_c = 0.001(8/3\sin^4(2\alpha - \pi/2)), \tag{19}$$

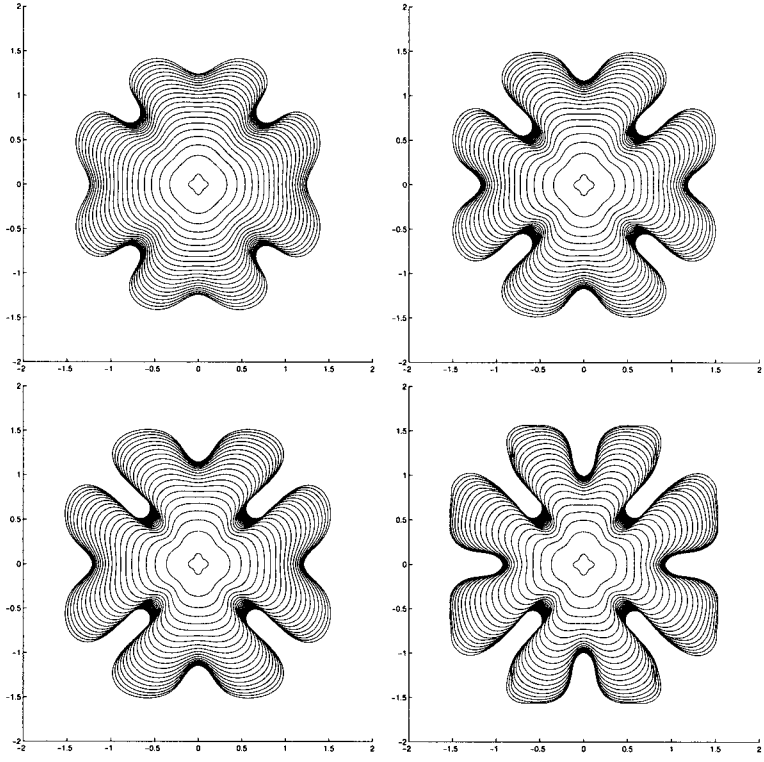

Fig. 4. Growth histories for four grid resolutions: from left to right and top to bottom, 120 points, 160 points, 200 points, 240 points in each spatial dimension. We apply the Gibbs–Thomson relation at the interface with $\epsilon_c = 0.002$ and $\epsilon_v = 0.002$. As we refine the grid the artificial numerical dissipation becomes negligible compared to the physical mechanisms and the zero level set of ϕ converges to a similar shape.

where α is the angle between the normal to the interface and the x-axis. This four-fold anisotropy will cause the crystal to grow along the four diagonal axes as detailed in [2]. Consider the initial seed to be an irregular pentagon on a domain $\Omega = [-1.5, 1.5] \times [-1.5, 1.5]$ on a grid with 200 points in each spatial dimension. We let the crystal grow to a final time $t_{\text{final}} = 0.4$. Figure 5 demonstrates that the crystal indeed grows along the preferred diagonal directions. Note that the dendrite growing from the initial singularity at the top corner of the pentagon is properly limited by the anisotropic surface tension that attains a maximum along the y-axis.

3.5. Grid Orientation Effects with Anisotropic Surface Tension

This test demonstrates that the artificial grid anisotropy is negligible. Consider a domain $\Omega = [-1, 1] \times [-1, 1]$ with 100 grid points in each spatial dimension on

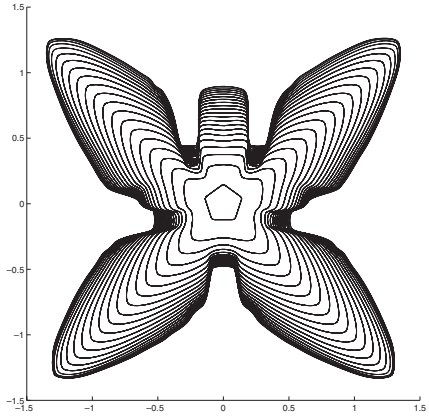

Fig. 5. Effect of anisotropic surface tension. The interface condition is the fourfold anisotropy boundary condition $T = -\epsilon_c \kappa$ with $\epsilon_c = 0.001(8/3 \sin^4(2\alpha - \pi/2))$. The crystal grows along the preferred diagonal directions and the dendrite growing from the initial singularity at the top corner of the pentagon is properly limited by the anisotropic surface tension that attains a maximum along the y-axis.

which we seed a crystal with initial shape described by the following parametric equation:

$$x(s) = 0.4 \cos(4s) \cos(s)$$
$$y(s) = 0.4 \cos(4s) \sin(s)$$

where $s \in [0, 2\pi]$. The interface condition is the fourfold anisotropy boundary condition $T = -\epsilon_c \kappa$ with $\epsilon_c = 0.001(8/3 \sin^4(2(\alpha - \alpha_0)))$, where α is defined as in Sec. 3.4 and α_0 is the preferred direction of growth. Figure 6a depicts the evolution of the level set function up to a time $t = 0.04$ when $\alpha_0 = 0$. The preferred directions are the x and y axes where the dendrite tips sharpen. On the diagonal axes, the surface tension at the interface attains a maximum value that forces the dendrite tips to widen. Figure 6b illustrates the evolution of the same initial data when $\alpha_0 = \pi/4$. The preferred directions are along the diagonal directions as expected. Moreover, the shape is that of Fig. 6a rotated by $\pi/4$ demonstrating that the artificial grid anisotropy is negligible. In this example, we compute the normal velocity component in four different coordinates directions as detail in [5].

3.6. Effect of Varying the Thermal Conductivity

This example illustrates the impact of varying the thermal conductivity. The velocity at the interface is given by $V_n = [v \nabla T \cdot \vec{n}]$, so the stronger the thermal conductivity v, the faster the growth. Here we consider a domain $\Omega = [-0.5, 0.5] \times [-0.5, 0.5]$ with 100 grid points in each direction. The initial data is given by the following parametric equations:

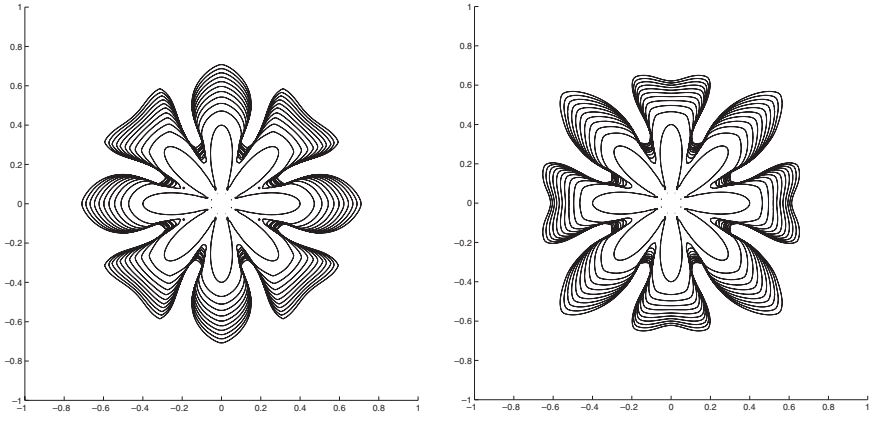

Fig. 6. Grid orientation effects with anisotropic surface tension on a grid with 100 points in each spatial dimension. The interface condition is the fourfold anisotropy boundary condition $T = -0.001(8/3 \sin^4(2(\alpha - \alpha_0)))\,\kappa$ with (left) $\alpha_0 = 0$ and (right) $\alpha_0 = \pi/4$. The shape of the crystal in the right figure is that of the crystal in the left figure rotated by $\pi/4$ demonstrating that the artificial grid anisotropy is negligible.

$$x(s) = 0.2(0.5 + 0.2\sin(6s))\cos(s)$$
$$y(s) = 0.2(0.5 + 0.2\sin(6s))\sin(s)$$

where $s \in [0, 2\pi]$ and we let the crystal grow to a final time of $t = 0.025$. In this example we impose the condition $T = -\epsilon_c \kappa$ at the interface with $\epsilon_c = 0.001$. Figure 7 depicts the results with two different values of the thermal conductivity v.

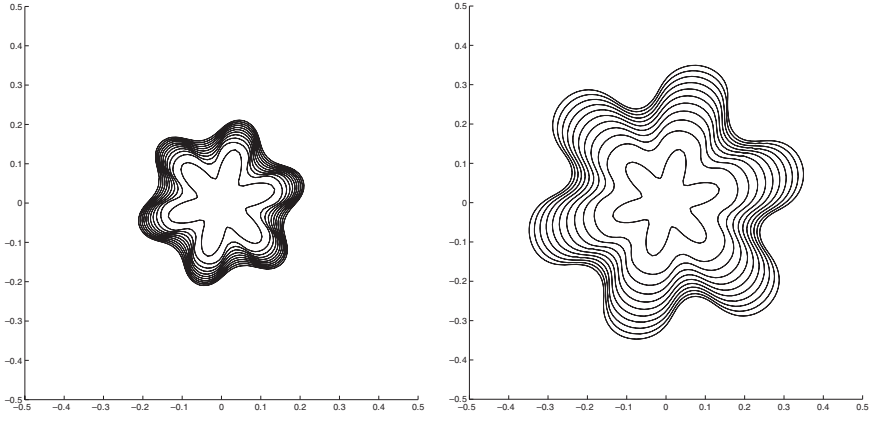

Fig. 7. Effect of varying the thermal conductivity on a grid with 100 grid points in each spatial dimension. This demonstrates that the interface velocity $V_n = [v\,\nabla T \cdot \vec{n}]$ is larger for higher value of the thermal conductivity. $v = 0.5$ for the left figure and $v = 1$ for the right figure.

3.7. Different Diffusion Constants

One advantage of using a level set formulation is the ability to simulate the growth of a crystal with a different thermal conductivity than the medium that it is in. This illustrates the versatility of our level set approach. The phase-field formulation, on the other hand, requires one to perform asymptotic expansion to include different thermal conductivity on each side of the front. Consequently, this has been a challenge up to recently [19].

We consider the same problem as in Sec. 3.6 but with different thermal conductivities on each side of the interface. Figure 8 depicts the results when the thermal conductivity inside $v_r = 1$ and the thermal conductivity outside $v_u = 1.2$. Note that in our approach the two-phase problem is separated into two distinct one since we impose a Dirichlet condition at the interface of each sub-domain. Therefore, one could take the ratio v_r/v_u as large as wanted and the algorithm would perform as well in contrast with phase-field. We have chosen a more subtle difference in the ratio to fit the results in the graph. In [21], the authors also studied discontinuous thermal conductivities with their non symmetric level set approach and showed that their numerical results converged to the linearized solvability theory of Barbieri and Langer [3].

3.8. Comparison to Solvability Predictions

An often used example to test the validity of the phase-field approach is to compute the dendrite tip velocity and tip shape of the standard fourfold anisotropy crystalline growth. Consider a domain $\Omega = [-8, 8] \times [-8, 8]$ with a grid spacing $\Delta x = 0.01$. We seed a disk of radius 0.15 in an undercooled bath with temperature $T_{\text{undercool}} = -0.65$. We impose the Gibbs–Thomson relation 5 at the interface with $\epsilon = 0.05$, $d_0 = 0.01$ and $\epsilon_v = 0$. The dimensionless tip velocity $\widetilde{V}_{\text{tip}} = V_{\text{tip}} d_0 / D$ reaches

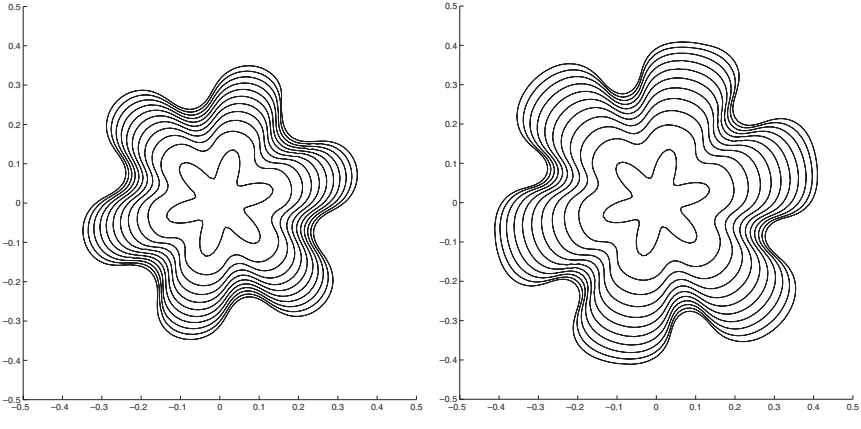

Fig. 8. Effect of having different thermal conductivity on each side of the interface on a grid with 100 grid points in each spatial dimension. The final time is 0.025. From left to right: $v_r = 1$ and $v_u = 1$, $v_r = 1$, and $v_u = 1.2$.

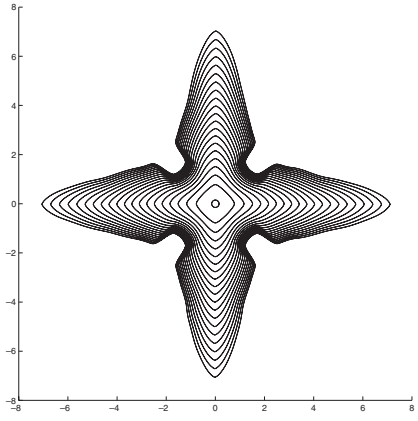

Fig. 9. Sequence of dendritic shapes in the case of standard fourfold anisotropy. The solution is computed on a $[-8,8]\times[-8,8]$ domain with 400 points in each directions, the undercooling is -0.65 and the anisotropy strength is given via the Gibbs–Thomson relation $T_I = 0.01(1-0.75\cos 4\alpha)$, where α is the angle between the normal to the interface and the x-axes. The final time is $t = 1.42$.

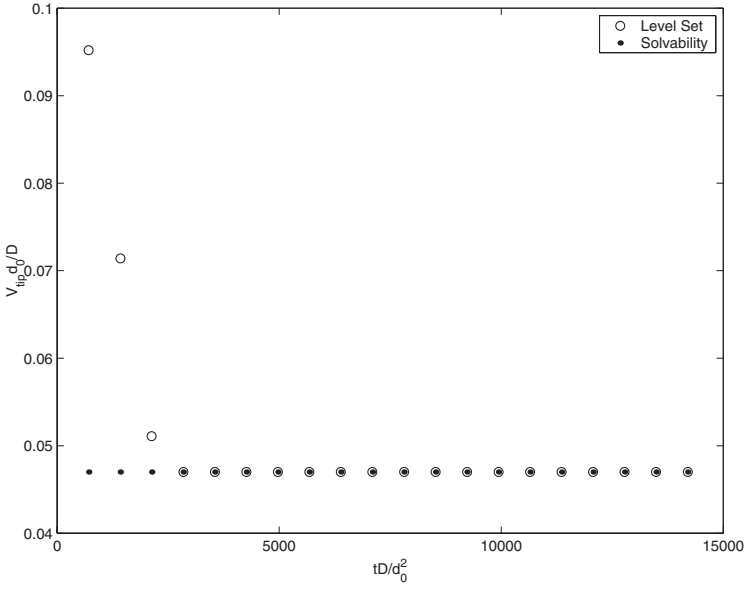

Fig. 10. Time evolution of the dimensionless tip velocity in the case of standard fourfold anisotropy. The solution is computed on a $[-8,8]\times[-8,8]$ domain with 400 points in each directions, the undercooling is -0.65 and the anisotropy strength is given via the Gibbs–Thomson relation $T_I = 0.01(1-0.75\cos 4\alpha)$, where α is the angle between the normal to the interface and the x-axes. The final time is $t = 1.42$. The dimensionless tip velocity $\tilde{V}_{\text{tip}} = V_{\text{tip}} d_0/D$ reaches a steady state value of 0.047 consistent with solvability theory.

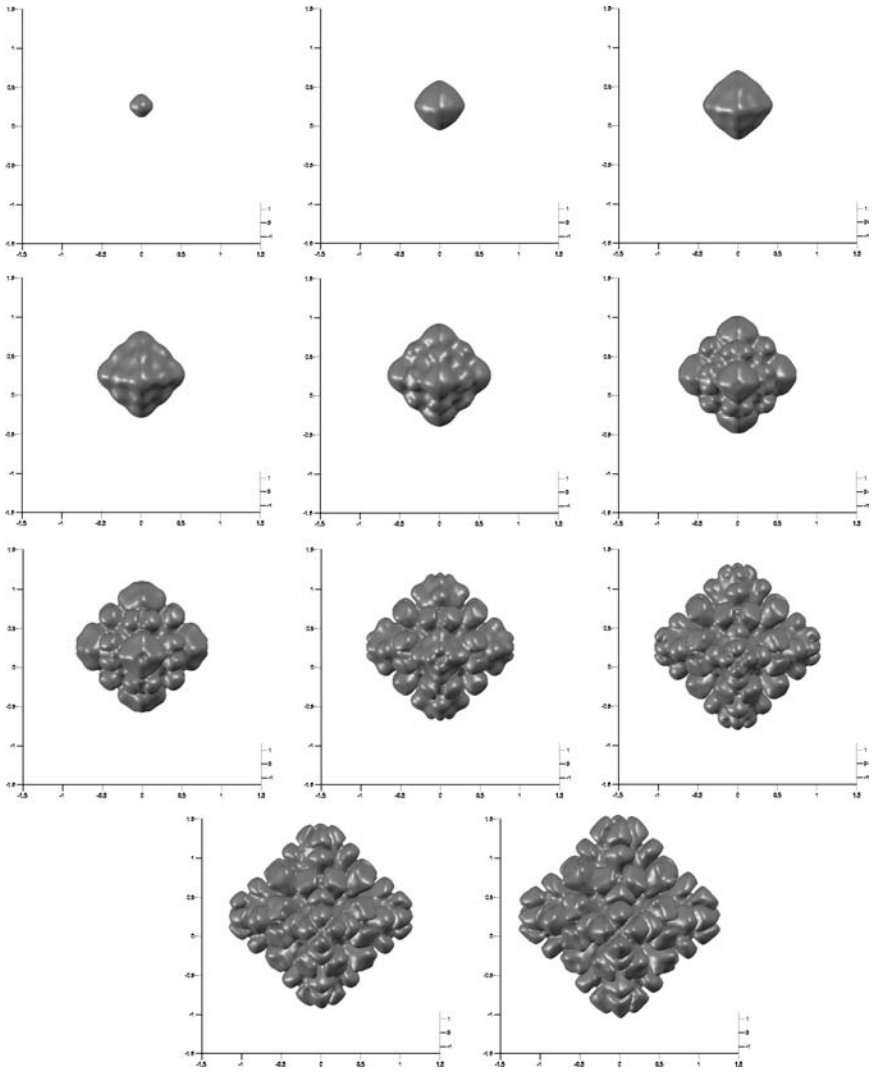

Fig. 11. 3D Stefan problem. The contours show the evolution of the interface location from time $t = 0$ s (top left) to $t = 0.14$ s (bottom right). We apply the Gibbs–Thomson relation at the interface with $\epsilon_c = 0.002$ and $\epsilon_v = 0.0.002$. This computation uses 100 grid points in each spatial direction.

a steady state value of 0.047 consistent with solvability theory (see Fig. 10) and Fig. 4 illustrates the dendritic shapes of the standard fourfold anisotropy.

3.9. Dendritic Growth in 3D

The following example illustrates our method's potential for modeling crystal growth in three spatial dimensions. We obtain a fair amount of detail in the dendrite structures with little computational effort, since our method yields a symmetric linear system that can be inverted efficiently (numerical experiments were performed on a Pentium III laptop).

Let $\Omega = [-1.5, 1.5] \times [-1.5, 1.5] \times [-1.5, 1.5]$. The initial data is given by $\phi = \min(\phi_1, \min(\phi_2, \min(\phi_3, \min(\phi_4, \min(\phi_5, \phi_6)))))$, where the ϕ_i's are spheres of radius 0.1 and centered off the x-axis or y-axis or z-axis by ± 0.05. Initially, $T = 0$ inside Ω^-, and $T = -0.5$ outside Ω^-. Dirichlet boundary conditions of $T = -0.5$ are enforced on $\partial\Omega$. We apply the Gibbs–Thomson relation, Eq. (5), at the interface with $\epsilon_c = 0.002$ and $\epsilon_v = 0.002$. The evolution of this initially "bumpy" sphere is presented in Fig. 11. The snapshots are given every 0.014 s from the initial time $t = 0$ s to the final time $t = 0.14$.

4. CONCLUSION

In conclusion, the level set method should be considered as a method of choice for the study of dendritic crystallization. We have shown that our algorithm can produce accurate solutions that can be compared favorably with solvability theory. In addition, our spatial discretization of the temperature yields symmetric matrices for the implicit time discretization that can be inverted with fast linear solvers, making it very efficient.

ACKNOWLEDGMENTS

F.G. was supported in part by an NSF postdoctoral fellowship # DMS-0102029, a Focused Research Group Grant # DMS0074152 from the NSF and by ONR N00014-01-1-0620. R.F. was supported in part by an ONR YIP and PECASE award N00014-01-1-0620 and NSF-0106694. R.C. was supported in part by a Focused Research Group Grant # DMS0074152 from the NSF. S.O. was supported in part by ONR N00014-97-0027 and NSF DMS-0074735.

REFERENCES

1. Adalsteinsson, D., and Sethian, J. (1999). The fast construction of extension velocities in level set methods. *J. Comput. Phys.* **148**, 2–22.
2. Almgren, R. (1993). Variational algorithms and pattern formation in dendritic solidification. *J. Comput. Phys.* **106**, 337.
3. Barbieri, A., and Langer, J. (1989). Predictions of dendritic growth rates in the linearized solvability theory. *Phys. Rev. A.* **39**, 5314.
4. Caflisch, R., Gyure, M., Merriman, B., Osher, S., Ratsch, C., Vvedensky, D., and Zinck, J. (1999). Island dynamics and the level set method for epitaxial growth. *Appl. Math. Lett.* **12**, 13.

5. Chen, S., Merriman, B., Osher, S., and Smereka, P. (1997). A simple level set method for solving Stefan problems. *J. Comput. Phys.* **135**, 8.
6. Chen, S., Merriman, B., Kang, M., Caflisch, R., Ratsch, C., Cheng, L.-T., Gyure, M., Fedkiw R., Anderson, C., and Osher, S. (2001). Level set method for thin film epitaxial growth. *J. Comput. Phys.* **167**, 475–500.
7. Chorin, A. (1985). Curvature and solidification. *J. Comput. Phys.* **58**, 472.
8. Enright, D., Fedkiw, R., Ferziger, J., and Mitchell, I. (in press). A hybrid particle level set method for improved interface capturing. *J. Comput. Phys.*
9. Enright, D., Marschner, S., and Fedkiw, R. (2002). Animation and rendering of complex water surfaces, SIGGRAPH 2002. *ACM Trans. on Graphics* **21**, 736–744.
10. Fedkiw. R. *A Symmetric Spatial Discretization for Implicit Time Discretization of Stefan Type Problems*, unpublished, June 1998.
11. Fedkiw, R., Aslam, T., Merriman, B., and Osher, S. (1999). A non-oscillatory Eulerian approach to interfaces in multimaterial flows (the ghost fluid method). *J. Comput. Phys.* **152**, 457.
12. Gibou, F., Fedkiw, R., Cheng, L.-T., and Kang, M. (2002). A second order accurate symmetric discretization of the poisson equation on irregular domains. *J. Comput. Phys.* **176**, 205.
13. Golub, G., and Van Loan, C. (1989). *Matrix Computations*, The Johns Hopkins University Press, Baltimore.
14. Harabetian, E., and Osher, S. (1998). Regularization of ill-posed problems via the level set approach. *SIAM J. Appl. Math.* **58**, 1689.
15. Jiang, G.-S., and Peng, D. (2000). Weighted ENO schemes for Hamilton–Jacobi equations. *SIAM J. Sci. Comput.* **21**, 2126–2143.
16. Jiang, G.-S., and Shu, C.-W. (1996). Efficient implementation of weighted ENO schemes. *J. Comput. Phys.* **126**, 202–228.
17. Juric, D., and Tryggvason, G. (1996). A front tracking method for dendritic solidification. *J. Comput. Phys.* **123**, 127.
18. Karma, A., and Rappel, W.-J. (1997). Quantitative phase-field modeling of dendritic growth in two and three dimensions. *Phys. Rev. E.* **57**, 4323.
19. Karma, A. (2001). Phase-field formulation for quantitative modeling of alloy solidification. *Phys. Rev. Lett.* **87**, 11.
20. Merriman, B., Bence, J., and Osher S. (1994). Motion of multiple junctions, a level set approach. *J. Comput. Phys.* **112**, 334.
21. Kim, Y.-T., Goldenfeld, N., and Dantzig, J. (2000). Computation of dendritic microstructures using a level set method. *Phys. Rev. E.* **62**, 2471.
22. Liu, X-D., Fedkiw, R., and Kang, M.-J. (2000). A boundary condition capturing method for Poisson's equation on irregular domain. *J. Comput. Phys.* **160**, 151–178.
23. Liu, X-D., Osher, S., and Chan, T. (1996). Weighted essentially non-oscillatory schemes. *J. Comput. Phys.* **126**, 200–212.
24. Osher, S., and Fedkiw R. (2001). Level set methods: An overview and some recent results. *J. Comput. Phys.* **169**, 475.
25. Osher, S., and Fedkiw, R. (2002). *Level Set Methods and Dynamic Implicit Surfaces*, Springer-Verlag, New York.
26. Osher, S., and Sethian, J. (1988). Front propagating with curvature-dependent speed: Algorithms based on Hamilton–Jacobi formulation. *J. Comput. Phys.* **79**, 12.
27. Petersen, M., Ratsch, C., Caflisch, R., and Zangwill, A. (2001). Level set approach to reversible epitaxial growth. *Phys. Rev. E.* **64**, 061602.
28. Ratsch, C., Gyure, M., Caflisch, R., Gibou, F., Petersen, M., Kang, M., Garcia, J., and Vvedensky, D. (2002). Level-set method for island dynamics in epitaxial growth. *Phys. Rev. B.* **65**, 195403.
29. Saad, Y. (1996). *Iterative Methods for Sparse Linear Systems*, PWS publishing company, Boston.
30. Sussman, M., Smereka, P., and Osher, S. (1994). A level set approach for computing solutions to incompressible two-phase flow. *J. Comput. Phys.* **114**, 146.
31. Zhao, H.-K., Chan, T., Merriman, B., and Osher, S. (1996). A variational level set approach to multiphase motion. *J. Comput Phys.* **127**, 179.